J. Fluid Mech. (2002), *vol.* 463, *pp.* 241–258. © 2002 Cambridge University Press
DOI: 10.1017/S0022112002008765 Printed in the United Kingdom

Self-similar enstrophy divergence in a shell model of isotropic turbulence

By M. V. MELANDER AND B. R. FABIJONAS
Department of Mathematics, Southern Methodist University, Dallas, TX 75243, USA

(Received 31 May 2001 and in revised form 20 December 2001)

We focus on the early evolution of energy E and enstrophy Z when the dissipation grows in significance from negligible to important. By considering a sequence of viscous shell model solutions we find that both energy and dissipation are continuous functions of time in the inviscid limit. Inviscidly, Z takes only a finite time t^* to diverge, where t^* depends on initial conditions. For viscous solutions, Z peaks long after t^*, but the inflection point for $Z(t)$ provides an excellent approximation to t^*. Near t^*, all of our high Reynolds number solutions obey the formula $\nu^{\alpha}\mathrm{d}Z/\mathrm{d}t = F(\nu^{\beta}Z)$. Neither the function F nor the constants α and β depend on initial conditions. We use F to obtain the inviscid limit. The energy spectrum remains concave down on double logarithmic scales until t^*. At t^*, the spectrum becomes algebraic at high wavenumbers, i.e. $E(k,t^*) \sim C_0k^{\sigma}$. Crucially, the spectral slope σ is steeper than $-5/3$. Thus, we conclude that the inviscid singularity at t^* is not associated with the establishment of a semi-infinite Kolmogorov range. For viscous solutions, the $-5/3$ range builds gradually after t^* starting from high wavenumbers, and Z peaks when the inertial range reaches the integral scale. Thus, the formation of the inertial range is a viscous process in our shell model.

1. Introduction

Three-dimensional turbulent flows dissipate energy. This dissipation is related to the enstrophy via the equation $\mathrm{d}E/\mathrm{d}t = -\nu Z$. The dissipation does not become less significant the higher the Reynolds number (e.g. the smaller the viscosity). On the contrary, observations suggest a finite limit for dissipation when the Reynolds number approaches infinity (Sreenivasan 1984). Moreover, at high Reynolds numbers, a laminar flow with vorticity usually does not stay laminar for long, but quickly becomes turbulent and thus energy dissipating. On phenomenological grounds, we therefore expect that Z becomes unbounded in the limit of vanishing viscosity. In addition, we may suspect that Z diverges within a finite time. This plausible inviscid singularity in Z is called the 'enstrophy divergence' or the 'energy catastrophe;' see Lesieur (1990).

Enstrophy divergence occurs in models of isotropic turbulence, the simplest case being the constant-skewness model for inviscid flow:

$$\frac{\mathrm{d}Z}{\mathrm{d}t} = csZ^{3/2}. \tag{1.1}$$

Here c is a positive numerical constant, and s is the velocity-derivative skewness factor, which measures vortex stretching in the flow. By assuming that s is constant in (1.1), we obtain enstrophy divergence of the form

$$Z = \frac{4}{c^2 s^2 (t - t^*)^2}, \quad t < t^* = \frac{2}{cs\sqrt{Z(0)}}. \tag{1.2}$$

If s depends on time but remains finite and positive then Z still diverges within a finite time. This result follows from rewriting (1.1) as an equation for $Z^{-1/2}$ and integrating; for details see Lesieur, p. 149. The literature puts the value of s at 0.3–0.5 for isotropic turbulence (Batchelor 1960, p. 118) and at 0.7 for atmospheric data (Wyngaard & Tennekes 1970). However, it is uncertain if those values of s remain valid in the inviscid limit. Thus, we cannot use them to conclude that the enstrophy blows up in the Euler equations. In fact, whether the Euler equations lose regularity in a finite time or not is a difficult and unsolved mathematical problem. For an introduction to this problem we refer to Frisch (1995, p. 115), and Dombre & Pumir (1994). Recent numerical work on finite time singularities in the Euler equations includes Pelz (2001). In the present paper, we do not address the regularity question for the Euler equations, but scaling laws in a particular shell model of turbulence. Without question, enstrophy divergence occurs in our model. Our task is to analyse this divergence.

Enstrophy divergence also occurs in the closure model EDQNM in the limit of zero viscosity; see Lesieur p. 183 and Andre & Lesieur (1977). In particular, Lesieur describes how finite energy dissipation in turbulent flows is consistent with a Kolmogorov range $E(k) \propto k^{-5/3}$ extending to all high wavenumbers when $\nu \to 0$. The corresponding enstrophy spectrum then diverges as $Z(k) \propto k^{1/3}$. The dissipation, of course, cuts the inertial range off near the dissipation scale so that the integral over $Z(k)$ remains finite when $\nu \to 0$. Lesieur points out that the inviscid enstrophy divergence may occur precisely as the inertial range stretches out to infinite wavenumbers. Briefly, we can state the argument as follows. Assume that a finite section of $k^{-5/3}$ range has formed and remains at a stationary level. Also, assume a constant energy flux toward higher wavenumbers. Because the integral of $E(k) \propto k^{-5/3}$ converges, only a finite amount of energy can fit under the inertial range at high wavenumbers. The constant energy flux supplies that amount of energy in a finite time. So the extension of the inertial range to infinity occurs in a finite time. According to Lesieur, this scenario is consistent with EDQNM calculations. For viscous calculations with the same initial conditions, Z then will peak at a time t' near t^* when the inviscid singularity occurs; see Lesieur p. 153.

In this paper, we examine the enstrophy divergence using Zimin's shell model (V. Zimin personal communication 1994; Zimin & Hussain 1995) rather than EDQNM. Important conceptual differences separate these two models as they are constructed to model different aspects of turbulence. Usually, the solutions to the two models are not directly comparable. EDQNM is a closure model and thus describes the evolution of an ensemble average whereas Zimin's model, like other shell models, describes single realizations (Lorenz 1972). EDQNM makes statistical assumptions to close the Kármán–Howard equation, which is an exact equation for isotropic turbulence. In contrast, shell models model the Navier–Stokes equations in wavenumber space, but make no statistical assumptions. Solutions to EDQNM are regular because they represent ensemble averages of all realizations. However, solutions to shell models are typically chaotic because they represent individual realizations. Such chaotic solutions produce jagged energy spectra different from the smooth spectra of EDQNM. The chaotic motion in a shell model contains the turbulence statistics, albeit not for the Navier–Stokes equations. One obtains the evolution of ensemble averages by averaging over a statistically significant ensemble of shell model solutions. By drawing out the differences between closure models and shell models, we do not claim one model is closer to reality than the other. On the contrary, the two modelling approaches are complementary.

The fundamental difference between Zimin's shell model and EDQNM is not at all obvious from the energy spectra presented in Zimin & Hussain (1995). In fact, their spectra look like EDQNM spectra. The reason for this similarity is that only solutions on a special manifold in the shell model were considered. On this manifold, solutions are not chaotic and they converge toward a similarity solution (with two characteristic length scales – the integral and dissipation scales) much like EDQNM. However, the full version of Zimin's shell model has two variables per shell rather than one as in Zimin & Hussain (1995). For the full model, typical solutions are chaotic as in other shell models. In our work presented here, we need not consider ensemble averages. To analyse the enstrophy divergence, individual realizations suffice for two reasons. First, the chaotic motion that requires ensemble averaging does not start until after t^*; see Melander (1997). Secondly, our shell model, like other shell models, has an inviscid fixed point corresponding to the Kolmogorov inertial range. In fact, the special manifold considered in Zimin & Hussain (1995) is precisely the stable manifold for this fixed point. The fact that the fixed point is an attractor on the stable manifold explains the absence of chaotic behavior in Zimin & Hussain (1995). More importantly, solutions starting from initial conditions near the stable manifold follow this manifold until they are close to the fixed point. Only then do they turn away from the manifold and become chaotic. Thus, the stable manifold determines the early evolution of the shell model solutions.

The organization of the paper is as follows. We begin in § 2 by reviewing Zimin's shell model and justifying our use of this model. In § 3, we examine the dependence of $Z(t)$ on the viscosity ν for fixed initial conditions. In § 4, we complete our study of $Z(t)$ by examining its dependence on initial conditions for a fixed value of ν. We incorporate results from § 3 to obtain a single first-order differential equation that describes the evolution of the enstrophy near t^*. Section 5 examines the skewness factor s near t^*, and § 6 describes the evolution of the energy spectrum near t^*. A comparison with EDQNM concludes the paper in § 7.

2. The shell model equations

Work on shell models began with Lorenz (1972), Gledzer (1973), Desnyansky & Novikov (1974) and Yamada & Okhitani (1987). Since then, a variety of shell models have been developed for the incompressible Navier–Stokes and other physical equations. In particular, the GOY model has been extensively studied with the focus being on anomalous scaling in fully developed turbulence, e.g. Jensen, Paladin & Vulpiani (1991). For an introduction to the subject of shell models we refer the reader to Bohr *et al.* (1998). We do not use the popular GOY model for reasons described below.

The present study is linked to an ongoing investigation into the classic problem of decaying isotropic turbulence. The primary aim of that investigation is to develop a theory for the inviscid limit of the decay. For this purpose, direct numerical simulations of the Navier–Stokes equations are not practical or even possible. Thus, we have chosen to use a shell model as our main computational tool. To our knowledge, Zimin's model is the only shell model that can currently address the decay problem. In contrast to other shell models, Zimin's includes the non-local interactions that are crucial in the decay problem. Starting from localized initial conditions in wavenumber space, the enstrophy divergence always precedes the general decay in the shell model. This occurrence of the enstrophy divergence motivates the present paper.

Zimin bases his model on a wavelet expansion of the Navier–Stokes equations very similar to the wave packet expansion of Nakato (1988). Modelling assumptions then reduce the number of variables in each wavenumber shell to just two 'collective' variables representing r.m.s. fluctuations of the wavelet amplitudes. Zimin's modelling assumptions, such as Brownian motion at each scale, are common in many disciplines of physics. Thus we may argue that Zimin's model at least in part rests on solid physical ground. In contrast, the GOY model has little rigorous basis.

We use Zimin's model as described in Zimin & Hussain (1995). There, one variable S_n characterizes the velocity fluctuations in the nth shell of wavenumbers $2^n\pi < k \leqslant 2^{n+1}\pi$. In this formulation, Zimin's model exhibits no chaotic behaviour and thus acts more like a closure model than a typical shell model. However, this resemblance with closure models is deceptive. In its full version, Zimin's model has two variables per shell: S_n and D_n (Zimin 1994, personal communication). It so happens that $D_n \equiv 0$ is a solution manifold; see equations below. Excluding forcing terms, the full equations for Zimin's model read

$$\frac{\mathrm{d}S_n}{\mathrm{d}t} = 2^{5n/2} \sum_{m=-\infty}^{\infty} T_m \left(\frac{S_n S_{n-m}}{2^{4m}} - \frac{D_n D_{n-m}}{2^{5m}} - 2^{3m/2} S_{n+m}^2 + 2^{3m/2} D_{n+m}^2 \right) - \nu 4^n 2\pi^2 S_n, \quad (2.1)$$

$$\frac{\mathrm{d}D_n}{\mathrm{d}t} = 2^{5n/2} \sum_{m=-\infty}^{\infty} T_m \left(\frac{S_n D_{n-m}}{2^{5m}} - \frac{D_n S_{n-m}}{2^{4m}} \right) - \nu 4^n 2\pi^2 D_n. \quad (2.2)$$

The model constants are as follows: $T_m = 0$ for $m < -1$, $T_{-1} = 0.1935$, $T_0 = 0$, and $T_m = 2^{5/2} T_{-1}$ for $m \geqslant 1$; ν is the kinematic viscosity. Note that T_{-1} is the only 'independent' constant; naturally, T_{-1} determines the Kolmogorov constant.

Expressions for energy E, enstrophy Z, helicity H, palinstrophy P, and the corresponding shell spectra E_n, Z_n, H_n and P_n are obtained directly from the shell amplitudes S_n and D_n as follows:

$$E \equiv \sum_n E_n, \quad E_n = \tfrac{1}{4}\rho_n (S_n^2 + D_n^2), \quad (2.3)$$

$$H \equiv \sum_n H_n, \quad H_n = 2\pi 2^n \rho_n S_n D_n, \quad (2.4)$$

$$Z \equiv \sum_n Z_n, \quad Z_n = \pi^2 4^n \rho_n (S_n^2 + D_n^2), \quad (2.5)$$

$$P \equiv \sum_n P_n, \quad P_n = 2\pi^4 16^n \rho_n (S_n^2 + D_n^2), \quad (2.6)$$

where $\rho_n \equiv 7\pi 8^n/18$. Note that (2.1), (2.2), and the derivative of (2.5) directly calculate $\mathrm{d}Z/\mathrm{d}t$ as well. The above expressions resemble expressions in Fourier modes of a velocity field; see for example Lesieur, p. 112. In fact, this resemblance becomes a perfect analogy once we make the following observations. First, Zimin's model builds on discrete wavelets rather than Fourier modes. Thus, summations replace integrals over wavenumbers. In addition, the density ρ_n of wavelets at scale n occurs in the summations. Second, we must use the discrete wavenumber $K_n = \sqrt{2}\pi 2^n$ rather than the continuous k in Fourier formulas like $Z(k) = k^2 E(k)$. Finally, the shell model uses the complex helical-wave decomposition (Lesieur, p. 98). In fact, S_n and D_n relate to fluctuations in the sum and difference of the complex helical modes $u^+(\boldsymbol{k})$ and $u^-(\boldsymbol{k})$ in the nth shell.

By construction, the inviscid shell model has a fixed point corresponding to the Kolmogorov inertial range. That fixed point is $(S_n, D_n) = (S_0 2^{-11n/6}, 0)$, where S_0 is a constant. Note that the inviscid shell model is invariant under the transformation $(t, S_n, D_n) \rightarrow (-t, -S_n, -D_n)$, so the sign of S_0 is important for the stability of the fixed point. A linear stability analysis of the fixed point reveals strictly non-zero real eigenvalues. All stable eigenmodes have $D_n \equiv 0$ when $S_0 < 0$; all unstable modes have $D_n \equiv 0$ when $S_0 > 0$. Thus the fixed point is an attractor on the manifold $D_n \equiv 0$ when $S_0 < 0$. The fixed point is a very special inviscid solution. Not only does $\mathrm{d}S_n/\mathrm{d}t = 0$, but the term behind the summation sign in (2.1) itself vanishes for each *m*. Because of this 'local' cancellation, viscous solutions on the manifold $D_n \equiv 0$ can lock on to $(S_n, D_n) = (S_0 2^{-11n/6}, 0)$ over a finite range of shells. Consequently, we find a viscous similarity solution with a clean inertial range. All numerical evidence shows attraction to this similarity solution from everywhere on the manifold $D_n \equiv 0$. Thus, we conclude that $D_n \equiv 0$ is the stable manifold for the fixed point and also for the viscous similarity solution. We note that the stable manifold is free of helicity in all shells (see equation (2.4)). Any perturbation off the manifold $D_n \equiv 0$ injects helicity into some shells. Such perturbations immediately destroy the viscous similarity solution and lead to chaotic behaviour (Melander 1997). We then only recover the Kolmogorov inertial range after ensemble averaging.

The numerical solution of the shell model equations requires careful treatment. In particular, our least-viscous calculations require the use of 128-bit arithmetic or quadruple precision. We effectively simulate the infinite range of shells by allocating many more shell variables than become dynamically significant during our calculations. For example, our least-viscous calculation dynamically engaged about 50 shells out of 91 allotted. In fact, shells at the ultraviolet extreme never gain any energy, while the shell at the infrared extreme carry less than $3 \times 10^{-31}\,\%$ of the total energy. We used the same large range of shells for all calculations presented in this paper. The computational burden of including these inactive shells in the calculation is insignificant. We note that the main computational effort occurs near t^* where very short time steps are necessary. Moreover, we need a stiff solver to compute to t^* and beyond. In fact, both VODE (Brown, Byrne & Hindmarsh 1989) and RADAU5 (Hairer & Wanner 1991) successfully integrate our shell model within a few minutes, whereas the non-stiff solver RKSUITE (Brankin, Gladwell & Shampine 1991) fails near t^*. VODE is, in contrast to RADAU5, readily adapted to quadruple precision. Thus, VODE serves as our integrator for the present paper. Note that we integrate the full shell model equations (2.1) and (2.2). Because we use the variables S_n and D_n the numerical implementation inherits the stable manifold $D_n \equiv 0$ exactly. Thus, the numerical solution stays on this manifold regardless of the inevitable round-off errors. Finally, we note that trajectories off the stable manifold consume much more computer time and are probably impossible to compute at the high Reynolds numbers reported in this paper.

3. Scaling laws

The following two equations are exact for isotropic turbulence:

$$\frac{\mathrm{d}E}{\mathrm{d}t} = -\nu Z, \tag{3.1}$$

$$\frac{\mathrm{d}Z}{\mathrm{d}t} = \left(\frac{98}{270}\right)^{1/2} s Z^{3/2} - \nu P. \tag{3.2}$$

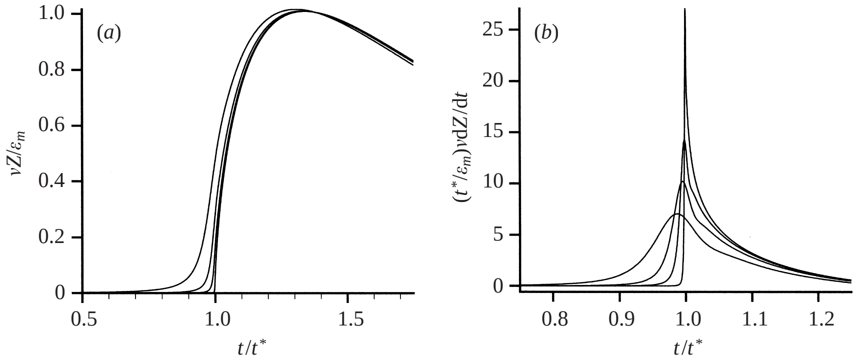

FIGURE 1. (*a*) The energy dissipation νZ is shown for four values of the viscosity, $\nu = 7.70 \times 10^{-2}$, 7.70×10^{-3}, 7.70×10^{-4} and 7.70×10^{-5}. In all cases the evolution starts from the same initial conditions; #2 in table 1 (§4). The figure suggests that the dissipation has a well-defined inviscid limit. For normalization we use the inviscid singularity time t^* and the maximum value ε_m of the dissipation in the inviscid limit. (*b*) The rate of change of the dissipation is shown for corresponding values of ν. We observe divergence at t^*.

See e.g. Lesieur, p. 146. These equations are also exact for our shell model. We know neither the skewness factor s nor the palinstrophy P in terms of E and Z. Therefore, we cannot in principle solve the equations for Z without making modelling assumptions. Our objective is not to introduce such assumptions, but to analyse the individual terms in the equations as time passes t^*. For this purpose, our numerical shell model solutions allow us to calculate any term in the above equations (see equations (2.3)–(2.6)). As an example, figure 1 shows the behaviour of the dissipation and its derivative as time passes t^* for different values of ν.

In our viscous calculations, the intrinsic Reynolds number

$$R_\lambda = \frac{E}{\nu}\sqrt{\frac{20}{3Z}} \tag{3.3}$$

changes drastically near t^*. This is because the energy remains nearly constant while the enstrophy explodes. However, after Z has peaked at t', the Reynolds number varies only slowly, i.e. $R_\lambda \sim t^{-1/12}$ during the decay on the stable manifold; see Melander (1997). Due to the large variation of $R_\lambda(t)$ in our calculations, we quote three values: $R_\lambda(0)$ for the initial conditions; $R_\lambda(t')$ for the decay; and $R_\lambda(t'')$ at the inflection point for $Z(t)$. $R_\lambda(t'') \approx R_\lambda(t^*)$ shows the closest proximity to the inviscid singularity. For given initial conditions, the dependence on ν is as follows:

$$R_\lambda(0) \sim \nu^{-1}, \quad R_\lambda(t') \sim \nu^{-1/2}, \quad R_\lambda(t'') \sim \nu^{-0.62} \approx \nu^{-5/8}. \tag{3.4}$$

The second relation reflects that dissipation (νZ) has an inviscid limit. The third relation follows from results obtained later in this section.

Before we concentrate on t^*, let us consider the relationship between Z and $\mathrm{d}Z/\mathrm{d}t$ during a calculation that runs far into the decay regime. The relationship generally involves power laws and therefore is best viewed using double logarithmic axes. Figure 2 shows a typical example for evolutions on the stable manifold. The arrows on the graph follow the progress of time. Because the enstrophy increases before t' and decreases afterwards, we plot the absolute value of $\mathrm{d}Z/\mathrm{d}t$. The graph has a cusp where $\mathrm{d}Z/\mathrm{d}t$ changes sign; see (*d*) in figure 2. This cusp is a consequence of the logarithmic scale and is of no significance. Increasing enstrophy characterizes

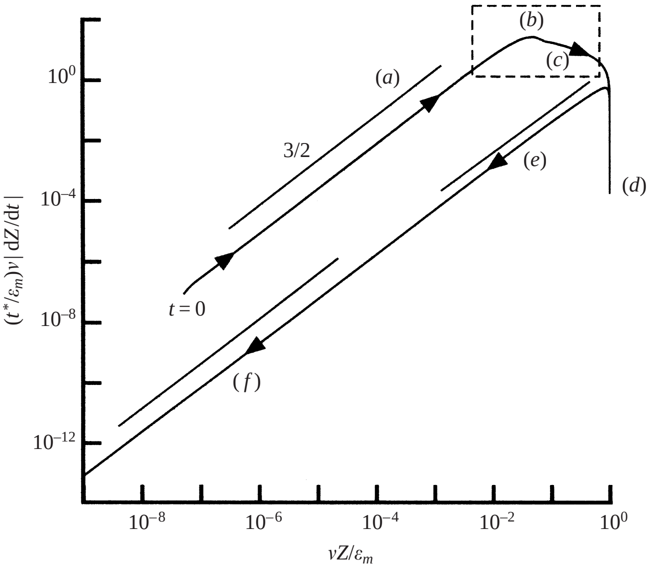

FIGURE 2. The evolution starting from initial condition #2 in table 1 for $\nu = 7.70 \times 10^{-5}$. The evolution progresses past t^* and runs deep into the regime of the asymptotic decay. We analyse the boxed part of the evolution. The letters along the curve refer to the discussion in the text.

the early evolution marked (a) in figure 2. The figure reveals a clear 3/2 slope, so we deduce from equation (3.2) that s is roughly constant and νP is insignificant at this stage. The inviscid evolution ends shortly before $Z(t)$ reaches its inflection point marked (b). From there the evolution enters a new power-law regime (c), which is of short duration and ends before Z peaks at (d). After (d) the enstrophy usually decays monotonically, but Z may peak again for some initial conditions. Before reaching the asymptotic decay law (f), we see a transitional period (e) whose duration varies with initial conditions. The decay exponent during this transitional period can differ significantly from the asymptotic value, which is independent of initial conditions (Melander & Fabijonas 2002, see also figure 4).

For the present investigation we focus on the boxed part of the evolution shown in figure 2. We are especially interested in what happens in the limit of zero viscosity. To address this question figure 3 shows the same evolution for a sequence of decreasing viscosities. The viscosity changes by a factor of 10 between neighbouring curves. In figure 3 we have multiplied both Z and $\mathrm{d}Z/\mathrm{d}t$ by ν on the assumption that the dissipation and its derivative have well-defined inviscid limits after t^*. This assumption is motivated by figure 1 and is supported by the fact that all curves coincide in the right-hand side of figure 3(a). Figure 3(a) reveals a well-defined slope A for the power law (c) in figure 2. We measure $A = -0.56$.

Between the power-law regimes (a) and (c) of figure 2 we have the transition (b) where Z and $\mathrm{d}Z/\mathrm{d}t$ scale in a non-trivial way with ν. Remarkably, a similarity technique eliminates ν from the transition: we can shift all the curves such that their transition zones coincide; see figure 3(b). Due to the logarithmic axes, the scaling $(\nu^{\alpha}\mathrm{d}Z/\mathrm{d}t, \nu^{\beta}Z)$ accomplishes the shifting for appropriate values of α and β. Thus, we claim that some dimensionless function F describes the transition:

$$\nu^{\alpha}\frac{\mathrm{d}Z}{\mathrm{d}t} = F(\nu^{\beta}Z). \tag{3.5}$$

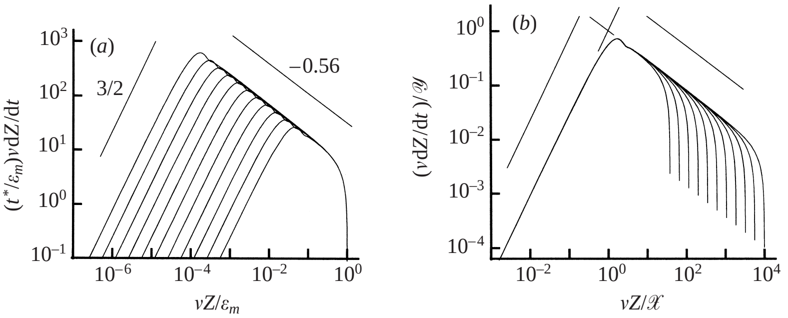

FIGURE 3. (*a*) The evolution starting from initial condition #2 in table 1 is shown as time passes t^* for $\nu = 7.70 \times 10^{-5}$, $\nu = 7.70 \times 10^{-6}, \ldots, \nu = 7.70 \times 10^{-15}$. The smallest ν corresponds to the leftmost curve. (*b*) The same curves shifted so that both asymptotes coincide; i.e. the crossing of the asymptotes in (*a*) provides the normalization factors $\mathscr{X} = \exp(X)$ and $\mathscr{Y} = \exp(Y)$, see equation (3.8). The smallest ν now corresponds to the rightmost curve. The figure reveals the existence of an inviscid limit.

Using figure 3(*a*), we calculate α and β in the following way. Each curve in the figure has a left and a right leg separated by a rounded corner. The corner corresponds to $t = t'' \approx t^*$ when $d^2E/dt^2 = -\nu dZ/dt$ peaks. Both legs are asymptotically straight lines with slopes that are independent of ν. The slope of the left leg is 3/2, and the right is A. Away from the corner the right legs coalesce into a single curve revealing that the dissipation νZ and its derivative have well-defined inviscid limits after t^*. Before t^*, the evolution is inviscid; therefore Z and dZ/dt evolve independent of ν. Consequently, the spacing between the legs is uniform in figure 3(*a*) (note that the figure shows $\nu dZ/dt$ versus νZ rather than dZ/dt versus Z). Applying the value 3/2 for the slope of the left leg, it is easy to show that the left legs shift as $\nu^{1/3}$. Using Cartesian notation to denote the lines in figure 3(*a*), the left leg falls on the line

$$Y = \tfrac{3}{2}(X - \log(\nu^{1/3})), \tag{3.6}$$

while the asymptote for the right leg is

$$Y = A(X - X_0). \tag{3.7}$$

The two lines cross at the point

$$\begin{pmatrix} X \\ Y \end{pmatrix} = \begin{pmatrix} -1/(2A-3) \\ -A/(2A-3) \end{pmatrix} \log \nu + \begin{pmatrix} 2AX_0/(2A-3) \\ 2A^2X_0/(2A-3) - AX_0 \end{pmatrix}. \tag{3.8}$$

For a given value of ν, this point is just above the corner of the curve in figure 3(*a*). When we shift from one curve to the next by changing ν, the point (X, Y) shifts as well. Thus, equation (3.8) provides the scaling coefficients α, β that make the curves coincide. Specifically, we obtain

$$\alpha = A/(2A-3) + 1, \tag{3.9}$$

and

$$\beta = 1/(2A-3) + 1. \tag{3.10}$$

We note that $\alpha = 3\beta/2$. For $A = -0.56$, we have $\alpha = 1.1359$ and $\beta = 0.7573$.

IC#	Signs of S_{-1}, S_0, S_1	t^*	$R_\lambda(t')$	$R_\lambda(t^*)$
1	$+++$	0.0270	1.20×10^5	6.92×10^5
2	$---$	0.0189	1.46×10^5	7.86×10^5
3	$+--$	0.0297	1.54×10^5	8.99×10^5
4	$-+-$	0.0165	1.13×10^5	5.95×10^5
5	$--+$	0.0188	1.44×10^5	7.69×10^5
6	$++-$	0.0281	1.44×10^5	7.80×10^5
7	$-++$	0.0164	1.09×10^5	6.29×10^5
8	$+-+$	0.0294	1.51×10^5	8.73×10^5

TABLE 1. Initial conditions (IC) for the shell model calculations. The non-zero amplitudes are: $|S_{-1}| = 72$, $|S_0| = 392$, and $|S_1| = 72$. The initial Reynolds number is the same in all cases, namely $R_\lambda(0) = 7.6 \times 10^8$.

Knowing α and β, we can draw important conclusions regarding the inviscid limit. First, $Z(t'') = O(\nu^{-\beta})$. Using that $t'' \to t^*$ as $\nu \to 0$, we obtain

$$\frac{\mathrm{d}E}{\mathrm{d}t} = -\nu Z = O(\nu^{1-\beta}) \quad \text{for} \quad \mathrm{t} \leqslant \mathrm{t}^*. \tag{3.11}$$

Since $1 - \beta > 0$, the dissipation vanishes before t^*. We expected this result, of course. The derivative of the dissipation is more exciting. We have $(\mathrm{d}Z/\mathrm{d}t)|_{t''} = O(\nu^{-\alpha})$ so that

$$\frac{\mathrm{d}^2E}{\mathrm{d}t^2} = -\nu\frac{\mathrm{d}Z}{\mathrm{d}t} = O(\nu^{1-\alpha}) \quad \text{at} \quad t = t^*. \tag{3.12}$$

This quantity blows up in the inviscid limit because $1 - \alpha \approx -0.13$ is negative. Thus $E(t)$ is differentiable once, but not twice. Later, in § 4 we will show that differentiability fails only at one instant, namely t^*.

4. Dependence on initial conditions

We obtained figure 3 using initial conditions with a sharply peaked spectrum. That is, only the three amplitudes S_{-1}, S_0, S_1 are non-zero. Energy, enstrophy and palinstrophy spectra involve the squared amplitudes; see equations (2.3)–(2.6). Thus, we can construct seven other initial conditions with the same spectra by varying the signs of S_{-1}, S_0, S_1.

The resulting evolutions differ drastically. The enstrophy diverges at a different time in each case; see table 1. The enstrophy also peaks at a different level in each case, as does $\mathrm{d}Z/\mathrm{d}t$. Moreover, the decay differs significantly between cases; see figure 4. Note that we observe a common asymptotic decay exponent ($\alpha_E \approx -7/6$) for the energy, but only after 99% of the energy is lost.

In contrast, all eight cases behave alike near t^*; see figure 5(a). In fact, we can shift the curves so that all eight coincide; see figure 5(b). The implication is that some dimensionless function G describes all eight cases:

$$B\frac{\mathrm{d}Z}{\mathrm{d}t} = G\left(\frac{Z}{C}\right). \tag{4.1}$$

Here B and C are constants specific to the initial conditions. The constants account for the shifts that make the curves coincide. We note that the left legs of the curves have a common asymptote. The shifts must be parallel to this asymptote. Since

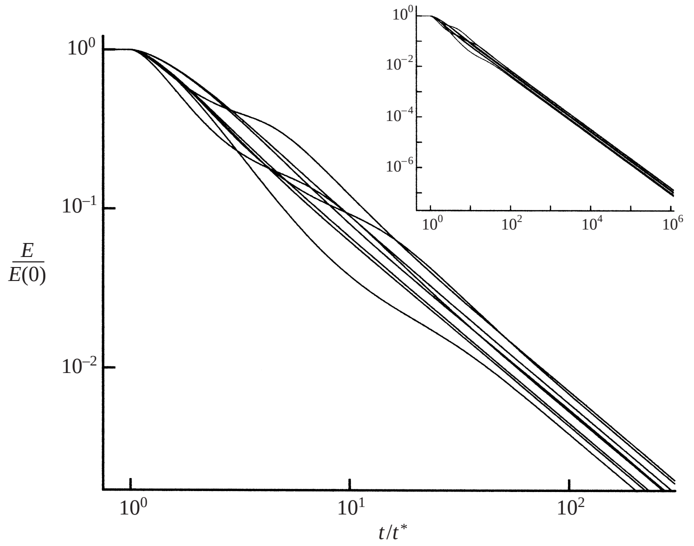

FIGURE 4. Energy decay during evolution of initial conditions listed in table 1. In all cases, $\nu = 7.70 \times 10^{-5}$. Although all cases eventually exhibit power laws with a common exponent, early transients can persist for a long time.

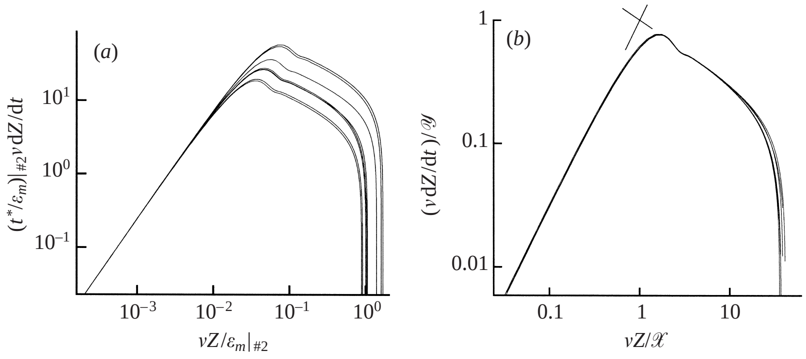

FIGURE 5. (*a*) Evolution of the eight initial conditions listed in table 1 for $\nu = 7.70 \times 10^{-5}$. Note that initial condition number two is used for normalization of all cases; this is done to keep the left legs coinciding. (*b*) The same curves shifted so that both asymptotes coincide.

the slope of the asymptote is 3/2, it follows that $B = C^{-3/2}$. We cannot state the dependence on the initial conditions in further detail. In particular, we cannot provide a formula for C in terms of initial conditions. This is in part because (4.1) is not valid until the enstrophy starts the $(t - t^*)^{-2}$ run, and that takes some time.

One initial condition (#2) is that used in § 3. Therefore, G is the same function as that describing the dependence on ν, i.e. $G = F$. We combine (3.5) and (4.1) to obtain

$$C^{-3/2}\nu^{3\beta/2}\frac{\mathrm{d}Z}{\mathrm{d}t} = F\left(\frac{\nu^{\beta}Z}{C}\right). \tag{4.2}$$

Using similarity variables

$$\tau = \left(\frac{C}{\nu^{\beta}}\right)^{1/2}(t - t^*) \tag{4.3}$$

and

$$\zeta = \frac{\nu^{\beta}}{C} Z, \tag{4.4}$$

equation (4.2) reduces to

$$\frac{\mathrm{d}\zeta}{\mathrm{d}\tau} = F(\zeta). \tag{4.5}$$

This formula describes the viscous evolution near t^* for all initial conditions and all small values of ν. In that sense, F is a universal function for the shell model.

Let $\Delta\tau$ be the 'similarity time' spent rounding the corner on the graph of F. According to (4.3), the corresponding 'physical time' is $\Delta t = \Delta\tau(\nu^{\beta}/C)^{1/2}$. Since β is positive, Δt shrinks to zero in the inviscid limit. Thus, the two asymptotic legs of F determine the inviscid limit of $Z(t)$. On the left leg $F(\zeta) = K\zeta^{3/2}$, where K is some numerical constant determined by how we normalize F. Solving for ζ, we obtain $\zeta = 4/(K^2\tau^2)$. We readily rewrite this expression as

$$Z = \frac{4}{K^2(t-t^*)^2}, \quad t < t^*. \tag{4.6}$$

Neither C nor ν appears in this formula. The only reference to the initial conditions is therefore through t^*. Similarly, on the right leg $F(\zeta) = \tilde{K}\zeta^{A}$, where $\tilde{K}$ is another numerical constant (related to K) again determined by the normalization of F. We solve for ζ and use (3.10) to obtain $\zeta = M\tau^{2/\beta-2}$, where M is a numerical constant. M depends only on A and $\tilde{K}$. Again we rewrite the solution using the original variables:

$$\nu Z = MC^{1/\beta}(t-t^*)^{2/\beta-2} \approx MC^{4/3}(t-t^*)^{2/3}, \quad t > t^*. \tag{4.7}$$

According to equations (3.11) and (4.7), the dissipation νZ has a well-defined inviscid limit $\varepsilon(t)$ both before and after t^*. Moreover, $\varepsilon(t)$ is continuous at t^*, but not differentiable there. The derivative of $\varepsilon(t)$ vanishes before t^*, but $\varepsilon(t)$ has a vertical asymptote from the right side of t^*. Thus, $\mathrm{d}\varepsilon/\mathrm{d}t$ is discontinuous and not defined at t^*; it is, however, defined everywhere else. Because of the discontinuity at t^*, the convergence $\nu\mathrm{d}Z/\mathrm{d}t \to \mathrm{d}\varepsilon/\mathrm{d}t$ is non-uniform. This clarifies what we see in figure 1(*b*).

We can only find F by solving the shell model equations. The required numerical calculations are not straightforward. In particular, it is necessary to use 128-bit arithmetic to reproduce the numerical results in the present paper. Various technical problems may arise in this connection, including the fact that not all ODE solvers produce accuracies consistent with 128-bit arithmetic. (We used the solver VODE by Brown *et al.* (1989)). To allow the reader to bypass these technical difficulties we present both a tabulation and a spline fit in table 2.

We fit $f \equiv \log_{10} F$ as a function of $x = \log_{10}\zeta$. That is, we fit the graph of F as it appears on double logarithmic axes like in figure 3(*b*). This graph is easy to fit due to the straight asymptotes. Our fit uses the B-spline representation

$$f(x) = \sum_{i=1}^{m-4} c_i N_i(x), \tag{4.8}$$

where $N_i(x)$ is the normalized cubic B-spline defined on the knots $\lambda_i, \lambda_{i+1}, \ldots, \lambda_{i+4}$ and m is the total number of knots. The first four knots are identical, and so are the last four. The spline coefficients are determined using the method of Dierckx (1975). Standard numerical software reproduces $f(x)$ from knots and coefficients; see Cox (1972). (We used routine E02BBF from the NAG library.) Our spline fit is graphically indistinguishable from the outermost curve in figure 3(*b*). Naturally, we

i	λ_i	c_i	$f(\lambda_i)$
1	−1.419192	−2.110824	
2	−1.419192	−1.798384	
3	−1.419192	−1.310180	
4	−1.419192	−0.668218	−2.110824
5	−0.786923	−0.287936	−1.183519
6	−0.437064	−0.133485	−0.703656
7	−0.033788	−0.176705	−0.259045
8	0.169455	−0.289218	−0.156832
9	0.302857	−0.317946	−0.203074
10	0.396939	−0.327974	−0.286902
11	0.460200	−0.365825	−0.316456
12	0.517565	−0.481182	−0.332549
13	0.550899	−0.797038	−0.346404
14	0.715778	−1.090908	−0.424479
15	1.243444	−1.283891	−0.705607
16–19	2.275448	2.118210	−1.283891

TABLE 2. Knots and coefficients for the spline reconstruction of F.

have normalized F as in figure 3(*b*). That is, the crossing of the asymptotes is at the origin, thus allowing easy renormalization. To shift $f(x)$ horizontally, we subtract a constant from all knots. To shift $f(x)$ vertically, we subtract a constant from all coefficients. The vertical shift works because the splines form a partition of unity:

$$\sum_{i=1}^{m-4} N_i(x) = 1.$$

5. The skewness factor

We calculate the skewness factor s using equation (3.2). From our numerical solution of equations (2.1) and (2.2), we know all quantities in (3.2) other than s. Instantaneous data thus yield

$$s = \left(\frac{270}{98}\right)^{1/2} \left(\frac{\mathrm{d}Z}{\mathrm{d}t} + 2\nu P\right) Z^{-3/2}. \tag{5.1}$$

This formula eliminates numerical differentiation from the post-processing of our numerical shell model solution. We use no ensemble averaging in the calculation of s because we only consider realizations on the stable manifold (those are not chaotic). Below, we examine the variation of s with Reynolds number, time and initial conditions.

Figure 6(*a*) shows the evolution of s at various Reynolds numbers for fixed initial conditions. We observe that s converges to a well-defined inviscid limit before t^*. Sometime after t^* however, s has no inviscid limit. In fact, we find that at times much larger than t^*

$$s = s_0 + A_0 \cos(\omega_0 \ln t + \phi), \tag{5.2}$$

where the constants s_0, A_0 and ω_0 have inviscid limits, but the phase ϕ does not. Near t^* the skewness factor fluctuates wildly, but in a surprisingly systematic way. In the inviscid limit, s becomes discontinuous at t^* with one oscillation before t^* and another after t^*. These oscillations are power laws in $|t - t^*|$ with purely imaginary

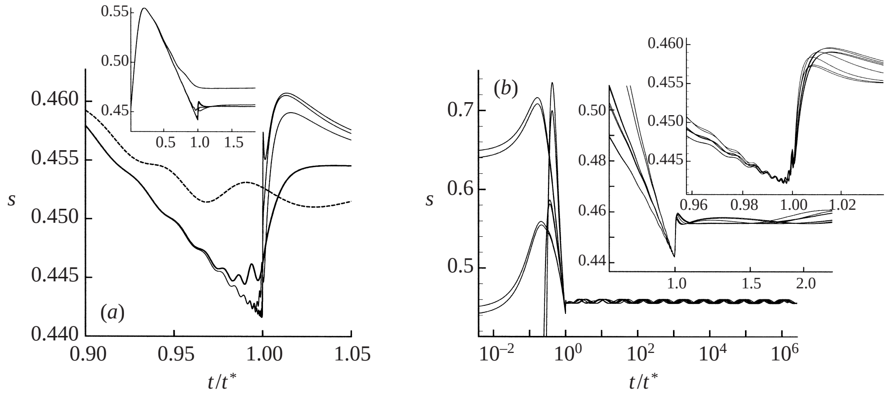

FIGURE 6. (*a*) The evolution of the skewness factor s for a sequence of increasingly smaller ν. The initial conditions are the same in all cases. (*b*) The skewness factor s for the eight initial conditions listed in table 1 for $\nu = 7.70 \times 10^{-5}$.

exponents. By replotting the data so the abscissa is logarithmic in $|t-t^*|$, we find that both amplitude and frequency are constants. We also find non-uniform convergence of the oscillations near t^* as $\nu \to 0$. The plot is rather complicated and not shown here.

Figure 6(*b*) illustrates the dependence on initial conditions. The eight initial conditions are those listed in table 1, so that the initial spectra are identical, but the phases of the shell variables differ. The initial Reynolds number is the same in all cases. Since t^* differs significantly among the eight evolutions, we have normalized t by t^*. The general comments made for figure 6(*a*) also apply here. In addition, we point to a common value of s near t^*. Moreover, the constants s_0, A_0 and ω_0 are the same for all cases, but the phase ϕ is not. At early times before t^*, the skewness factor varies substantially from case to case. Sometimes, s is even negative. This may seem unusual as s is normally assumed positive. The explanation lies in the fact that we are considering individual realizations rather than ensemble averages. Specifically, the inviscid shell model is invariant under the transformation $(S_n, D_n, t) \to (-S_n, -D_n, -t)$. Our selection of the initial conditions thus ensures that $\mathrm{d}Z/\mathrm{d}t$ is initially positive in half the cases and negative in the other half. With νP negligible at early times, s is proportional to $\mathrm{d}Z/\mathrm{d}t$ and can therefore be negative.

Overall, our results for the skewness factor compare favourably with the literature. As with EDQNM, s remains bounded during the divergence, and the inviscid limit is discontinuous at t^*. The size of s is also acceptable. Excepting the slow small-amplitude oscillation, s is constant after t^* as it should be for decaying turbulence; see Lesieur, p. 146. In addition, the early overshoot of s before t^* is a well-known phenomenon, e.g. (McComb 1996, p. 316). For comparison, we mention the recent calculations by Lesieur & Ossia (2000) which obtain the inviscid limit of s for EDQNM. The calculations show s increasing monotonically from near zero at $t = 0$ to a maximum of 1.132 near t^*. An abrupt drop then follows and s subsequently flattens at the constant value 0.547.

The small-amplitude oscillations are both a puzzle and a concern. We find them both near t^* and at late times. They also occur in $E(t)$ during the final $t^{-5/2}$ decay at very low Reynolds numbers. We do not know much about the oscillations, except that they are power laws in $|t-t^*|$ with imaginary exponents. One power law occurs before t^*, a second after t^*, and third at late times. Currently, it is unclear to us whether

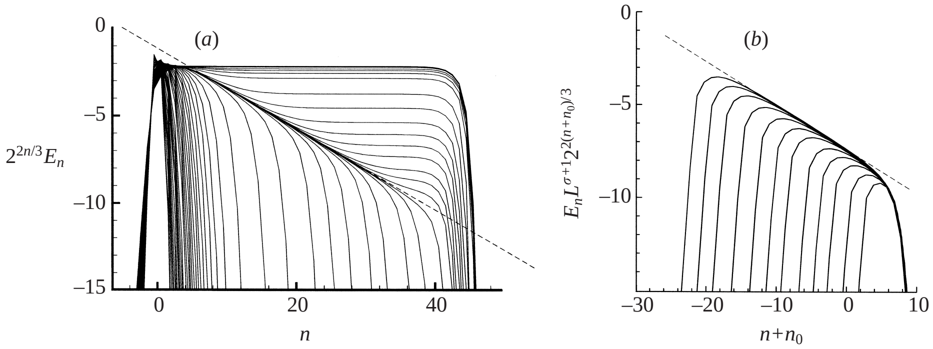

FIGURE 7. (*a*) The compensated energy spectrum at selected times in the interval $[0, t']$, mostly near t^*. The vertical scale is logarithmic with base 2, but otherwise arbitrary. The dashed line shows the spectral slope at t^*. Note that the computational range of shells is larger than shown in the figure. (*b*) Collapse of the spectral evolution before t^*; $n_0 = \log_2 L$ where L is given by equation (6.7).

the oscillations are just a peculiarity of our particular shell model or if they have some physical significance. We do know that the oscillations are part of the model and not numerical artifacts. Until other theoretical considerations support a physical interpretation, we are inclined to suspect the physical relevance of the oscillations. Note that ensemble averaging will take the oscillations out of the skewness factor. Unfortunately, ensemble averaging will also blur the behaviour of s during the enstrophy divergence as t^* varies with initial conditions.

6. The energy spectrum

The shell model spectrum E_n is discrete and thus differs from the continuous wavenumber spectrum $E(k)$. However, the two spectra are closely related. In fact, we may think of the discrete spectrum as obtained from the continuous spectrum by integrating one octave of wavenumbers. For an algebraic spectrum (e.g. $E(k) = k^m$), the spectral slope is therefore larger by 1 in the discrete case than in the continuous case, i.e.

$$\int_{2^n}^{2^{n+1}} k^m \, \mathrm{d}k \sim (2^n)^{m+1}. \tag{6.1}$$

In particular, the slope of the Kolmogorov inertial range is $-5/3$ for the continuous spectrum, but $-2/3$ for the shell spectrum.

We gain information about the formation of singularities from the high-wavenumber spectrum. Whenever the spectrum tails off algebraically, some regularity of the velocity field is lost. That is, the physical-space velocity field is differentiable only a finite number of times. In contrast, when the spectrum decays faster than algebraic at high wavenumbers the velocity field is differentiable arbitrarily many times. Thus, if the spectrum becomes algebraic at all high wavenumbers within a finite time, then derivatives beyond a certain order of the velocity field develop finite time singularities.

Figure 7(*a*) shows several snapshots of the compensated energy spectrum $2^{2n/3}E_n$ at times near t^* for our least-viscous calculation. The Kolmogorov inertial range is horizontal in this figure. We also note that the spectral evolution is from left to right. The dashed line corresponds to the first algebraic spectrum that forms during the evolution. Inviscidly, this algebraic spectrum produces a singularity and thus by definition forms precisely at t^*. The spectral slope is distinctively steeper than for the inertial range. In fact, figure 7(*a*) shows conclusively that the inertial range is absent before t^*. Therefore, the formation of the inertial range is not causing the enstrophy divergence. Figure 7(*a*) also reveals that the inertial range develops in the viscous regime of the calculation after t^*. The formation process starts at the high wavenumbers and gradually extends to the integral scale.

On the double logarithmic axes, the spectrum remains concave down until t^*. Moreover, the spectrum appears to evolve self-similarly at high wavenumbers. That is, the spectrum slides along the dashed line in figure 7(*a*) while keeping the same shape. This process forms the stationary algebraic spectrum (the dashed line in figure 7*a*) starting near the integral scale. Without viscosity, this algebraic spectrum reaches infinite wavenumbers precisely at t^*. This inspection suggests that we should look for a self-similar description of the high-wavenumber spectrum before t^*. We draw further support for this idea by using computer graphics to shift the individual spectra in the figure. In fact, we find that simple translations make the spectra collapse to a single curve representing the evolution at large wavenumbers. Thus, we may expect self-similarity in the form of power laws. Based on these observations, we analyse the inviscid evolution of the high-wavenumber spectrum in an idealized setting. For simplicity, we use the continuous wavenumber description (k) rather than the discrete one (shells).

We assume that the evolution at the integral scale can be separated from that at the high wavenumbers. This way, we may consider the low-wavenumber spectrum to be

$$E(k,t) \sim C_0 k^{\sigma} \quad \text{as} \quad k \to 0 \tag{6.2}$$

for the purpose of our high-wavenumber analysis. This asymptotic form then represents the straight section of the spectrum along the dashed line in figure 7(*a*). Guided by the figure, we furthermore assume that C_0 is independent of time. Since self-similarity of the energy spectrum implies self-similarity of the enstrophy spectrum, we use the fact that shifts make the spectra in figure 7(*a*) coincide and write

$$Z(k,t) = Z(t)L(t)J(kL(t)), \quad t < t^*, \tag{6.3}$$

where $L(t)$ is a typical length scale, and J a positive function with normalization

$$\int_0^{\infty} J(x)\,\mathrm{d}x = 1. \tag{6.4}$$

We can now derive two expressions for the enstrophy contained in scales larger than L. On the one hand we have

$$\int_0^{1/L} Z(k,t)\,\mathrm{d}k = Z(t)\int_0^{l} J(x)\,\mathrm{d}x = C_1 Z(t), \tag{6.5}$$

where C_1 is a positive numerical constant less than 1. On the other hand, we find

$$\int_0^{1/L} Z(k,t)\,\mathrm{d}k = \int_0^{1/L} k^2 E(k,t)\,\mathrm{d}k = \int_0^{1/L} C_0 k^{\sigma+2}\,\mathrm{d}k = \frac{C_0}{\sigma+3}L^{-\sigma-3}. \tag{6.6}$$

Using that $Z(t) = C_2(t-t^*)^{-2}$ before t^*, we can solve for L:

$$L \propto (t^* - t)^{2/(\sigma+3)}. \tag{6.7}$$

These expressions allow us to describe the inviscid energy spectrum before t^*. We have

$$E(k,t) = Z(k,t)/k^2 = Z(t)L^3 J(kL)/(kL)^2 \tag{6.8}$$

so that the energy spectra collapse to a single curve when plotting $E(k,t)(t^* - t)^{2\sigma/(\sigma+3)}$ versus $k(t^* - t)^{2/(\sigma+3)}$. The corresponding formula for the shell spectrum calls for plotting $E_n(t^* - t)^{(2+2\sigma)/(\sigma+3)}$ against $n + (2/(\sigma + 3))\log_2(t^* - t)$. Figure 7(*b*) shows the compensated spectrum before t^* in collapsed form. In this figure, the spectral evolution is from right to left.

Exactly at t^*, the energy spectrum becomes algebraic: $E(k,t^*) = C_0 k^\sigma$ for all k. Thus for $t < t^*$ we calculate the amount of additional energy that can still fit under the spectrum $C_0 k^\sigma$ as

$$E_a = C_4 \int_{1/L}^{\infty} C_0 k^\sigma \,\mathrm{d}k \propto L^{-\sigma-1}, \tag{6.9}$$

where C_4 is another numerical constant. Since C_0 is independent of time, the energy accumulation at high wavenumbers comes from the flux through the spectrum

$$E_{flux} = -\frac{\mathrm{d}E_a}{\mathrm{d}t} \propto \frac{\mathrm{d}}{\mathrm{d}t} L^{-\sigma-1} \propto (t^* - t)^\xi$$

where

$$\xi = \frac{-2(\sigma+1)}{\sigma+3} - 1. \tag{6.10}$$

Note that the exponent ξ vanishes when $\sigma = -5/3$, but is positive when $\sigma < -5/3$. Using figure 7(*a*), and recalling that the spectral slope for the shell model is 1 larger than for the Fourier spectrum, we have $\sigma \approx -2/3 - 1 - 0.24 \approx -1.90$ and $\xi \approx 0.66$.

We learn two things from this analysis. First, the inertial slope $-5/3$ emerges at t^* if the spectrum is self-similar with a stationary asymptote on the left-hand side and also has constant energy flux. This is in line with Lesieur's analysis. Second, the fact the shell model builds a spectrum with a slope $\sigma - 1$ steeper than the Kolmogorov slope $-2/3$ means that energy flux is not constant before t^*. On the contrary, the energy flux vanishes at the singularity, i.e.

$$E_{flux} \propto (t^* - t)^\xi \approx (t^* - t)^{2/3}, \quad t < t^*. \tag{6.11}$$

7. Conclusion

We have presented a detailed investigation of the enstrophy divergence in the inviscid limit of Zimin's shell model. Inviscidly, the enstrophy is known to blow up in both shell and closure models. Thus, we do not draw conclusions regarding the existence of a finite time singularity for the Euler equations. Instead, we juxtapose our results with those obtained by Lesieur for EDQNM without helicity. Our shell model investigation considers the stable manifold for the Kolmogorov inertial range. On this manifold, the helicity permanently vanishes in all shells. As a result, the shell model exhibits no chaotic behaviour. Thus, we may compare individual solutions with those obtained via EDQNM. This situation is exceptional, because normally individual shell model solutions are chaotic and we must ensemble average before comparison with a closure model such as EDQNM can take place.

Some of our findings agree with EDQNM. For example, our skewness factor s compares well with EDQNM: s has similar size, and remains positive and finite at t^*. Moreover, we reproduce the discontinuity of s in the inviscid limit. Like EDQNM, we find inviscid expressions for the enstrophy proportional to $(t - t^*)^{-2}$ before t^*, and an inviscid limit for the dissipation after t^*.

Our most important results, however, disagree with EDQNM. For viscous cases, our enstrophy does not peak at or near t^* as in EDQNM; see Lesieur, p. 153. We trace the source of this difference to the evolution of the energy spectrum. The critical difference concerns the spectral slope of $E(k, t^*)$ in the inviscid limit. Lesieur suggests that a finite $(-5/3)$ Kolmogorov range forms before t^* and extends to infinity precisely as $t \rightarrow t^*$. In contrast, we find no Kolmogorov range before t^*. Exactly at t^*, we do find a semi-infinite algebraic spectrum in the inviscid limit, but the spectral slope is steeper than $-5/3$. Moreover, we find that the Kolmogorov range forms after t^*. The formation process is gradual. It starts at the high wavenumbers and progresses backwards through the spectrum. The enstrophy peaks when the formation process finishes. In Lesieur's scenario, that happens at t^*; in our case, it occurs much later. Another significant difference concerns the energy flux through the spectrum before t^*. Lesieur's scenario corresponds to a constant energy flux, but we find that it vanishes completely as $t \rightarrow t^*$. We may summarize these differences by noting that we have a 'softer' inviscid singularity at t^* than does Lesieur. In our case, the inviscid limit of the dissipation is continuous. In Lesieur's case, it jumps from zero to a finite value at t^*.

Parts of our analysis go beyond what is currently available for EDQNM. In particular, we are referring to the similarity formula (4.5) describing the viscous passage through t^*. Table 2 allows reconstruction of this formula through spline coefficients for the function F. Also, we present asymptotic formulas, including that for the inviscid limit of the dissipation (3.11) and (4.7). Finally, one might apply our spectral similarity formula (6.8) to check Lesieur's conjecture (a Kolmogorov range exactly at t^*) via direct numerical simulations. That is, one could assume self-similarity of the spectrum and use the formula to find the spectral slope σ.

Finally, we note that the energy spectrum changes very fast near t^*. One can therefore easily miss the events associated with the inviscid singularity. In fact, insufficient sampling of the spectral evolution will lead one to believe that the Kolmogorov range forms at t^*. This incorrect conclusion was drawn by Melander (1997). After considering the enstrophy evolution in recent EDQNM calculations (Lesieur & Ossia 2000, figure 3*b*) and comparing them with our shell model, we have some doubt whether the Kolmogorov range actually forms at t^* even in EDQNM. When plotted in the same way, the enstrophy evolution looks qualitatively the same for both models. Moreover, it appears that in EDQNM the energy catastrophe occurs near the inflection point for the enstrophy rather than near the peak value. That may suggest the spectral slope at t^* to be steeper that $-5/3$ in EDQNM as well. Only a close examination of carefully sampled EDQNM spectra can address this issue.

REFERENCES

Andre, J. C. & Lesieur, M. 1977 Influence on helicity on high Reynolds number isotropic turbulence. *J. Fluid Mech.* **81**, 187–207.

Batchelor, G. K. 1960 *The Theory of Homogeneous Turbulence*. Cambridge University Press.

Bohr, T., Jensen, M., Paladin, G. & Vulpiani, A. 1998 *Dynamical Systems Approach to Turbulence*. Cambridge University Press.

Brankin, R., Gladwell, I. & Shampine, L. 1991 RKSUITE: a suite of Runge–Kutta codes for initial value problems for ODEs. *Tech. Rep.* SoftReport 91-S1. Dept. of Mathematics SMU, Dallas, TX, also in Netlib.

Brown, N., Byrne, G. & Hindmarsh, A. 1989 VODE: A variable coefficient ODE solver. *SIAM J. Sci. Statist. Comput.* **10**, 1038–1051.

Cox, M. 1972 The numerical evaluation of B-splines. *J. Inst. Math. Applics.* **10**, 134–149.

Desnyansky, V. & Novikov, E. 1974 The evolution of turbulence spectra to the similarity regime. *Izv. Akad. Nauk SSSR Fiz. Atmos. Okeana* **10**, 127–136.

DIERCKX, P. 1975 An algorithm for smoothing, differentiation and integration of experimental data using spline functions. *J. Comput. Appl. Math.* **1**, 165–184.

DOMBRE, T. & PUMIR, A. 1994 Singularities (and turbulence). In *Turbulence, A Tentative Dictionary* (ed. P. Tabling & O. Cardoso). Plenum.

FRISCH, U. 1995 *Turbulence*. Cambridge University Press.

GLEDZER, E. B. 1973 System of hydrodynamic type admitting two quadratic integrals of motion. *Sov. Phys. Dokl.* **18**, 216–217.

HAIRER, E. & WANNER, G. 1991 *Solving Ordinary Differential Equations II*. Springer.

JENSEN, M., PALADIN, G. & VULPIANI, A. 1991 Intermittency in a cascade model for three-dimensional turbulence. *Phys. Rev.* A **43**, 798–805.

LESIEUR, M. 1990 *Turbulence in Fluids*, 2nd edn. Martinus Nijhoff.

LESIEUR, M. & OSSIA, S. 2000 3D isotropic turbulence at very high Reynolds numbers: EDQNM study. *J. Turb.* **1**, 007.

LORENZ, E. 1972 Low order models representing realizations of turbulence. *J. Fluid Mech.* **55**, 545–563.

MCCOMB, W. 1996 *The Physics of Fluid Turbulence*. Oxford University Press.

MELANDER, M. 1997 Helicity causes chaos in a shell model of turbulence. *Phys. Rev. Lett.* **78**, 1456–1459.

MELANDER, M. & FABIJONAS, B. 2002 Transients in the decay of isotropic turbulence. *Dept. of Mathematics, SMU, Internal Rep.*

NAKATO, T. 1988 Direct interaction approximation of turbulence in wave packet representation. *Phys. Fluids* **31**, 1420–1430.

PELZ, R. 2001 Symmetry and the hydrodynamic blowup problem. *J. Fluid Mech.* **444**, 299–320.

SREENIVASAN, K. 1984 On the scaling of the turbulent energy dissipation rate. *Phys. Fluids* **27**, 1048–1051.

WYNGAARD, J. & TENNEKES, H. 1970 Measurements of the small-scale structure of turbulence at moderate Reynolds numbers. *Phys. Fluids* **13**, 1962–1969.

YAMADA, M. & OKHITANI, K. 1987 Lyapunov spectrum of a chaotic model of three-dimensional turbulence. *J. Phys. Soc. Japan* **56**, 4210–4213.

ZIMIN, V. & HUSSAIN, F. 1995 Wavelet based model for small-scale turbulence. *Phys. Fluids* **7**, 2925–2927.